# Chapter 3

## *AgI/$CuWO_4$ Z-scheme photocatalysts for the degradation of organic pollutants*

## 3.1. Introduction

There are several methods for the remediation of organic pollutants in industrial effluent (Forgacs et al., 2004; Salazar et al., 2012; Sun et al., 2019). These processes may be classified into those that purify water by separating the pollutants and others that oxidize or degrade the harmful substances by chemical means. Among the latter, photocatalysis is a particularly green method. The ultimate objective is to develop photocatalysts that can oxidize or degrade (specific) organic pollutants using only light and water (Kumar et al., 2014; Pirhashemi & Habibi-Yangjeh, 2017; Vasilaki et al., 2017).

Pure-phase semiconductor materials with bandgaps in the UV/visible range have disadvantages like inadequate VB or CB positions, reactant adsorption issues, and charge recombination problems (Zhou et al., 2014). Heterostructures or nanocomposites having two semiconductors with staggered bandgaps are better and more stable photocatalysts. Different properties of each phase impart better charge separation and reactant adsorption behavior. Heterostructures can follow a p-n heterojunction mechanism or a Z-scheme mechanism. Z-scheme photocatalysts have a minimum of two components, both of which are either n-type or p-type. Oxidation occurs on the component with more positive VB, while reduction occurs on the phase with a more negative (or less positive) CB position. Thus, Z-scheme photocatalysts exhibit better reduction and oxidation driving forces than their pure component counterparts (Q. Li et al., 2018; Nam et al., 2015; Niu et al., 2020).

The present research is on fabricating a Z-scheme photocatalyst with $CuWO_4$ as the oxidizing component (Nam et al., 2015). The interest in $CuWO_4$ stems from it being an n-type semiconductor with a visible range of 2.2-2.4 eV bandgap. Furthermore, $CuWO_4$ is stable against photo corrosion in neutral conditions (Askari et al., 2020; Shekofteh-Gohari & Habibi-Yangjeh, 2016; Tang et al., 2016). There are a

few reports on using $CuWO_4$ for the aerobic photocatalytic degradation of organic pollutants. Its highly positive VB position (NHE scale) results in photo-excited holes with strong oxidation ability, particularly for water splitting (Nam et al., 2015; Niu et al., 2020). Since the CB position is in a positive region (NHE scale), one must combine it with another semiconductor in an appropriate Z-scheme architecture for sufficient reducing ability. From this perspective, $CuWO_4$ has been coupled with other semiconductors like $Bi_2S_3$ and $VO_2$ to obtain visible light Z-scheme photocatalysts with suitable band positions and enhanced activities (Askari et al., 2020; Dashtian et al., 2018). But only a small number of reports of this type have been published.

In contrast to $CuWO_4$, many Ag-based semiconductors like $Ag_3PO_4$ (X. Hong et al., 2012; $Ag_2CrO_4$ (Silva et al., 2016), and AgX (AgCl, AgBr, AgI) (Shi et al., 2013) have more negative CB positions. Among them, AgI is an n-type semiconductor with a visible range bandgap of 2.7-2.8 eV. The more negative CB position makes photo-generated electrons with strong reduction ability (Q. Wang et al., 2016; Wen et al., 2020). It has also been used to construct Z-scheme photocatalysts such as AgI/$WO_3$ (T. Wang et al., 2016), AgI/$BiVO_4$ (Chen et al., 2016), and so on. Nevertheless, no research has yet been reported on fabricating an AgI/$CuWO_4$ photocatalyst.

The present investigation fabricates AgI/$CuWO_4$ nanocomposites by a step-wise precipitation method. The prepared nanocomposites were characterized using powder X-ray diffraction (XRD, Transmission electron microscopy (TEM), and X-photoelectron spectroscopy (XPS). Photoluminescence (PL) spectroscopy was also carried out on the samples. Solid-state UV-visible spectroscopy revealed the optical bandgaps in the prepared materials. The photocatalytic properties of the nanocomposites were then tested for the degradation of ciprofloxacin (CIP) and rhodamine B (RhB). CIP is a hard-to-degrade (quinolone) antibiotic, and RhB is a dye

often used to test photocatalyst activities. Appropriate radical trapping experiments found the active species responsible for the aerobic degradation of these pollutants.

### 3.2. Experimental details

#### *3.2.1. Synthesis of AgI/$CuWO_4$*

The binary composite AgI/$CuWO_4$ was synthesized by precipitating AgI on the $CuWO_4$ nanoparticles. First, six millimoles of the $CuWO_4$ nanoparticles were dispersed in 100ml DI water. Then 3.6 millimole (or 10% by weight of the re-dispersed $CuWO_4$ nanoparticles) $AgNO_3$ was added to the $CuWO_4$ nanoparticle dispersion. The resulting mixture was agitated on a thermostatic shaker for 24 hours. This step was necessary to ensure the adsorption of $Ag^+$ ions on $CuWO_4$ nanostructures. Next 50ml KI solution (3.6 mmol) was added in a dropwise manner to this ($CuWO_4$) dispersion along with 4 hours of constant stirring. The (yellowish-green) precipitate obtained was washed several times with water and ethanol. The final product was dried in a vacuum oven at 60°C. The obtained nanocomposite sample was 10% AgI/$CuWO_4$. This nanocomposite sample was labeled as 1 A/C. Two more nanocomposite samples with 20 and 30% AgI loadings on $CuWO_4$ were also prepared and represented by 2 A/C and 3 A/C labels (Scheme 3.1).

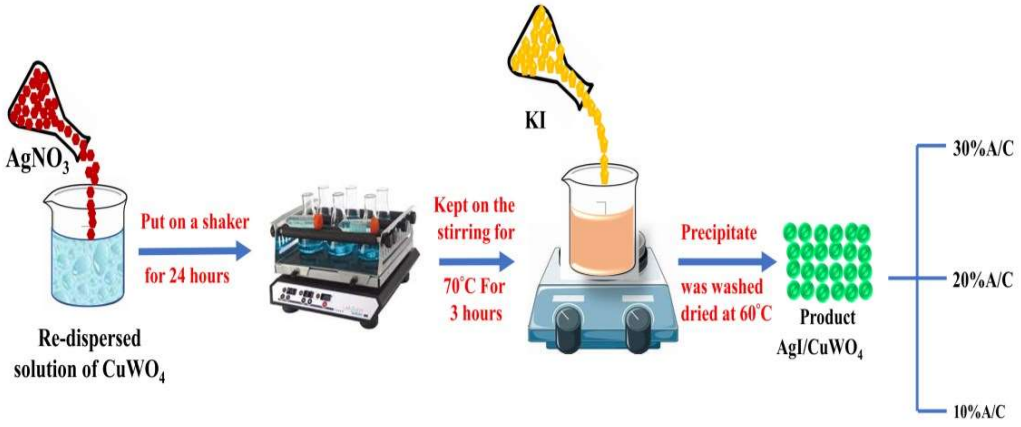


**Scheme 3.1:** A schematic of the AgI/$CuWO_4$ composite nanoparticle synthesis protocol

### *3.2.2. Photocatalysis experiments*

Photocatalytic degradation of RhB and CIP was carried out in the aqueous medium under a cool white LED light (1070 watts/meter$^2$). Precisely 200 $\mu L$ of a 0.5 mg/ml re-dispersed photocatalyst aqueous suspension was used for degrading ten ppm RhB and CIP solutions. In the reaction mixture (in a cuvette of 1cm in length), pH was adjusted to 3 and allowed to stand in the dark for 30 minutes until adsorption-desorption equilibrium. In this process, ~5-10% RhB/CIP is adsorbed on the photocatalyst surface. Note that the optimum pH of three was reached after experimenting with higher pH values. The photocatalytic degradation of the target molecule was monitored at regular intervals by UV-visible spectroscopy. The temperature of the chamber remained constant at 25°C. The following equation calculated the degradation percentage of the RhB and CIP.

$$\text{Removal Efficiency} = \left(\frac{C_o - C_t}{C_o}\right)x100 \qquad \text{---------- (3.1)}$$

In equation (3.1), the notation $C_0$ represents the initial concentration, and $C_t$ is the final concentration. For testing the reusability of the photocatalyst sample, after each run, the photocatalyst was recovered by centrifugation, rinsed with water, and dried at 60°C for 6 hours. The recovered (dried) photocatalyst was redispersed in an aqueous medium and used in the next run. Experimental conditions were identical in all cycles.

## 3.3. Results and Discussion

### *3.3.1. XRD pattern and Phase analysis*

Fig. 3.1 displays the XRD patterns of the powder samples of pure $CuWO_4$, AgI, and their composites (1 A/C, 2 A/C, and 3 A/C). The XRD pattern of the pure $CuWO_4$ (Fig. 3.1) agrees with its anorthic (triclinic) phase (P1- space group symmetry) as per JCPDS file 88-0269. The major peaks in this XRD are 15.3º, 19º, 28.7º, 30.1º, 31.6º, 32.1º, and 55.6° indexed to the (0 1 0) (1 0 0) ($\bar{1}$ $\bar{1}$ 1) (1 1 1) (0 2 0) ($\bar{1}$ 1 1) (1$\bar{1}$1) planes of $CuWO_4$, respectively (Gupta et al., 2019). Similarly, Fig. 3.1 is the XRD pattern of pure AgI prepared by the precipitation method. The spectrum matched with the face-centered cubic (FCC) phase (JCPDS

FILE No.78-0641) of AgI. XRDs of samples 1 A/C, 2 A/C, and 3 A/C showed peaks ascribed to triclinic $CuWO_4$ and FCC AgI (JCPDS FILE No. 87-26854) phases. The formation of both $CuWO_4$ and AgI phases indicates nanocomposite formation in all three samples.

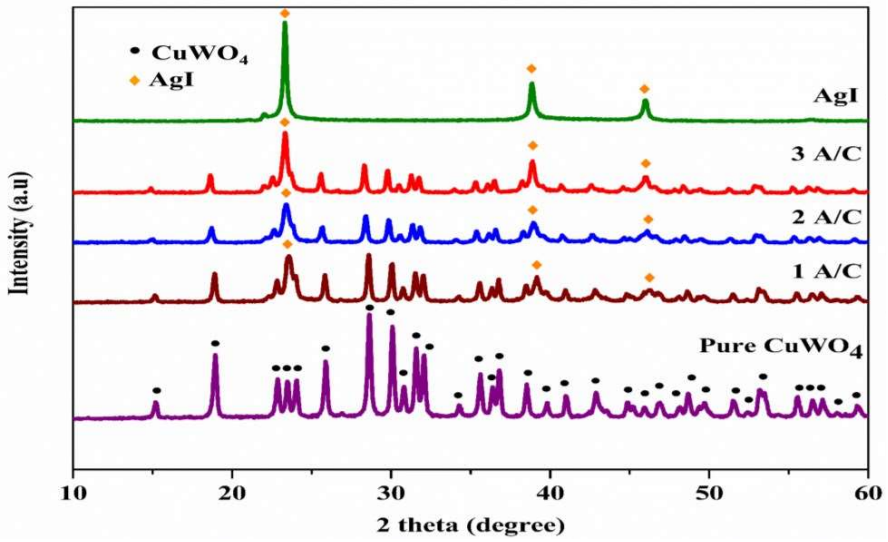


**Fig. 3.1:** Powder XRD diffraction patterns of the prepared materials $CuWO_4$, AgI, 1 A/C, 2 A/C, and 3 A/C

### *3.3.2. Morphology analysis through HR-TEM*

Fig. 3.2 shows TEM and HRTEM images of pure $CuWO_4$, 1 A/C, and 3 A/C nanoparticles. The nanostructures in Fig. 3.2a, 3.2c, and 3.2d are cubic or rectangular, with the HR-TEM fringe spacings (Fig. 3.2b) as per the $CuWO_4$ (100) plane. Fig. 3.3a presents the TEM image of the nanocomposite sample 2 A/C, showing spherical nanostructures superposed on particulates with cubic or rectangular morphologies. Fig. 3.3b gives the HRTEM of the 2 A/C sample. The HR-TEM (Fig. 3.3b) offers two types of fringe spacing matching the [110] and [200] planes of $CuWO_4$ and AgI phases on the same nanostructure. The adjacent locations of the two phases on the same particle confirm nanocomposite formation. The elemental mapping of the 2 A/C sample provides the same information (Fig. 3.3c). Elements present in AgI and $CuWO_4$ occupy adjacent places in these maps. Furthermore, the energy dispersive spectroscopy (EDS)

plots of samples show that the relative percentage of AgI increases as one progresses from 1 A/C, 2 A/C, and 3 A/C (Fig. 3.4).

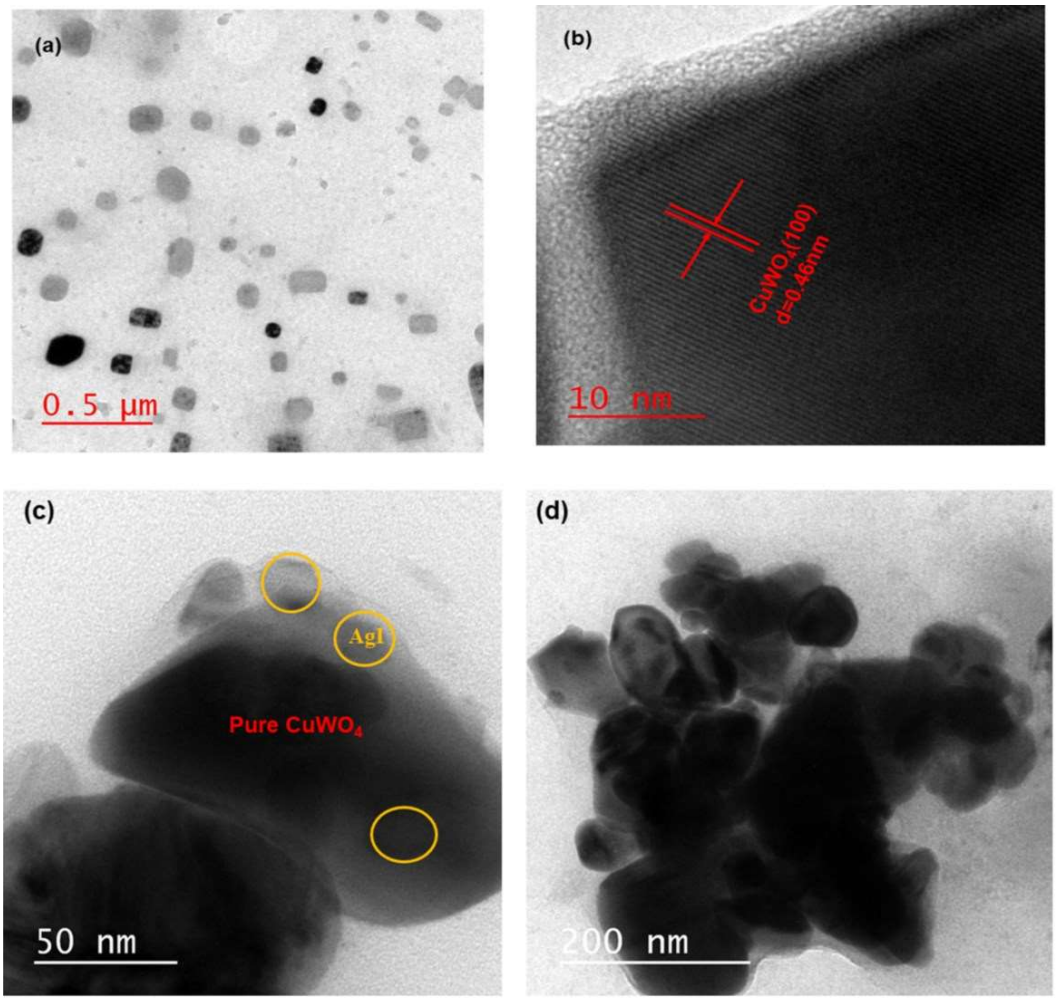


**Fig. 3.2:** TEM images of (a) Pure $CuWO_4$ and (b) shows HRTEM images of $CuWO_4$ (c) 1 A/C (d) 3 A/C

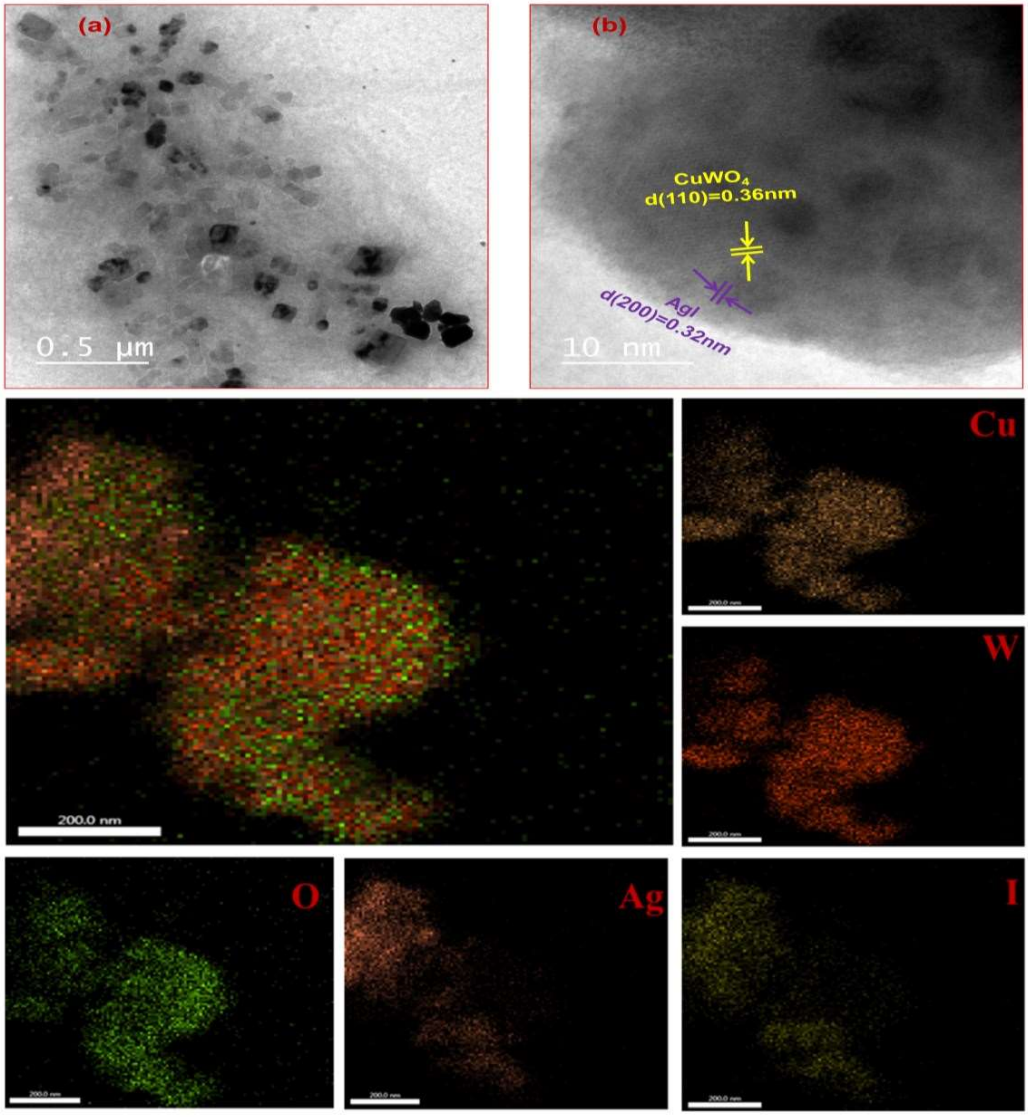


**Fig. 3.3:** (a) TEM and (b) HR-TEM images, and (c) elemental mapping of 2 A/C nanostructure

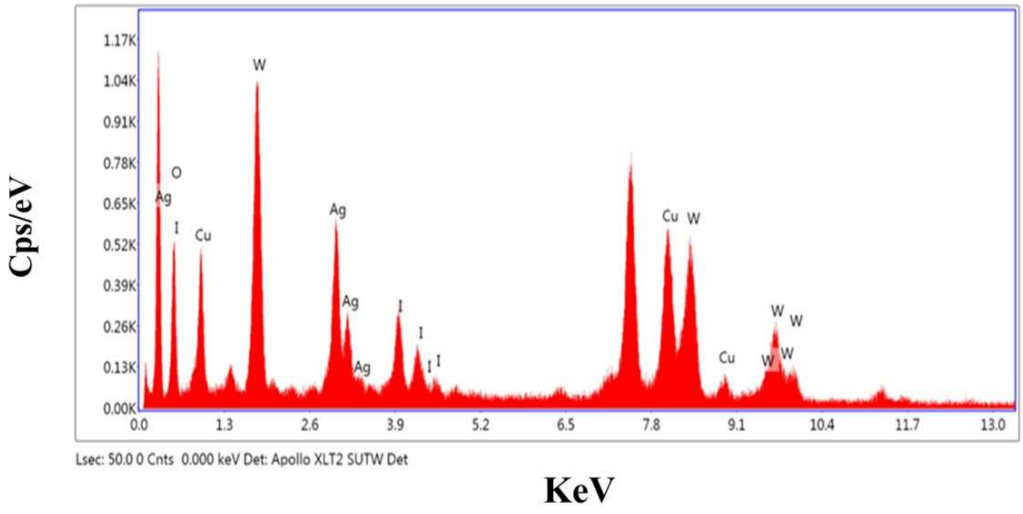


| Element | Weight % | Atomic % | Net Int. | Error % | Kratio | Z | R | A | F |
|---|---|---|---|---|---|---|---|---|---|
| O K | 48.80 | 86.91 | 102.19 | 9.52 | 1.0279 | 0.1660 | 1.0000 | 0.8497 | 0.3308 |
| Ag L | 21.95 | 5.80 | 247.37 | 6.06 | 0.9425 | 0.1657 | 1.0266 | 1.1765 | 0.7801 |
| I L | 15.41 | 3.46 | 139.67 | 11.15 | 0.9183 | 0.0864 | 1.0321 | 1.2247 | 0.5910 |
| Cu K | 5.73 | 2.57 | 445.97 | 7.61 | 0.9451 | 0.0261 | 1.1095 | 1.0261 | 0.4337 |
| W L | 8.11 | 1.26 | 411.09 | 3.94 | 0.9330 | 0.0996 | 1.1383 | 1.3802 | 1.1559 |

**Fig. 3.4:** Energy dispersive index (EDS) of 2 A/C catalyst

### *3.3.3. XPS characterization*

The XPS analysis helped us establish the composition and the oxidation states of elements in the nanocomposites (K. Li et al., 2019). Moreover, the joining of AgI and $CuWO_4$ shifted the binding energies of elements in the two phases (relative to the pure ones) to establish the operating Z-scheme mechanism (Xu et al., 2018). The binding energies of all elements were calibrated against C1s at 284.4 eV. The survey spectrum (Fig. 3.5f) of the 2A/C sample shows that the nanocomposite contains the elements Cu, W, O, Ag, and I. Fig. 3.5 compares the high-resolution XPS spectra of the pure $CuWO_4$ and AgI with various species in the 2A/C nanocomposite. Peaks corresponding to C2p,

W4f, O1s, Ag3d, and I3d appear in the XPS spectrum of the 2 A/C nanocomposite. The XPS spectrum of pure $CuWO_4$ exhibits Cu2p peaks belonging to $Cu^{2+}$ at 931.6 eV and 951.1 eV (attributed to $Cu2p_{3/2}$ and $Cu2p_{1/2}$, respectively). These $Cu2p_{3/2}$ and $Cu2p_{1/2}$ peaks also appear in the 2 A/C spectra at 933.8 and 954.1 eV, respectively. The Cu2p binding energies in the 2 A/C nanocomposite are higher than Cu2p values in the pure $CuWO_4$. While tungsten in the +6 state results in the two $Wf_{5/2}$, and $W4f_{3/2}$ peaks at 35.6 and 37.4 eV, similar peaks also appear in the 2 A/C spectrum. The $W4f_{3/2}$ binding energy moves to a slightly higher value of 37.6 eV. Then the O1s peak in pure $CuWO_4$ at 529.4 eV increases to 530.1 eV (O1s) in the spectrum of 2 A/C. Overall, most of the binding energy peaks of elements in $CuWO_4$ show a positive change. In contrast, the Ag3d binding energies of $Ag3d_{5/2}$ and $Ag3d_{3/2}$ at 368.5 and 374.5eV changed to 368.1 and 374.1 eV, respectively. Then $I3d_{5/2}$ and $I3d_{3/2}$ peaks at 619.7 and 631.4 eV (in the pure $CuWO_4$ sample) display a negative shift to 619.4 and 631 eV, respectively, in the 2 A/C nanocomposite. An increase in electron density on the AgI surface decreases the binding energies of elements in the AgI component of the 2 A/C composite. In contrast, increased binding energies of Cu, W, and O were caused by electron transfer away from the $CuWO_4$ surface. The overall migration of electrons from $CuWO_4$ to AgI points to a Z-scheme photocatalyst mechanism in the 2 A/C nanocomposite.

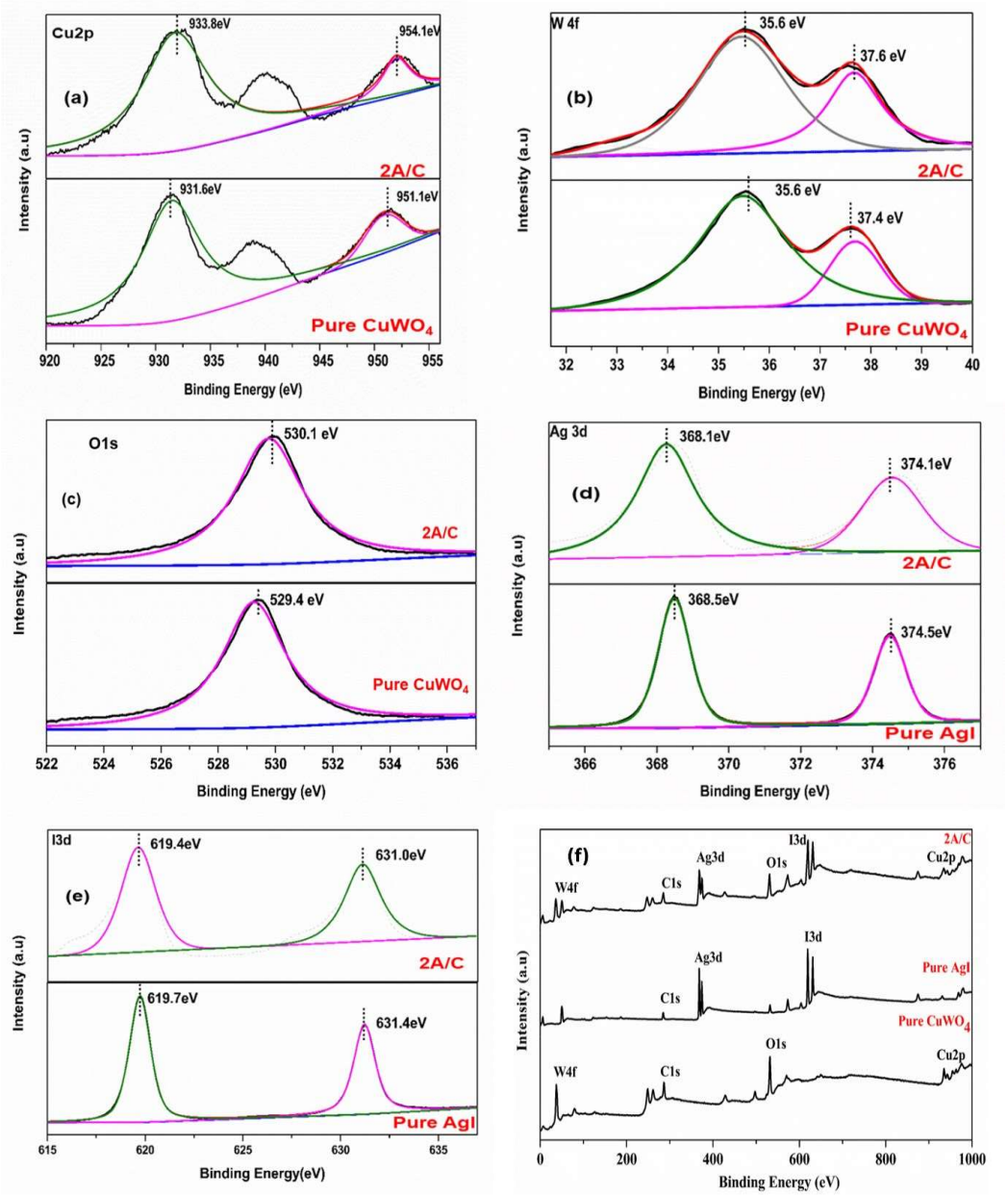


**Fig. 3.5:** Comparison of High resolution of XPS spectra (a) Cu 2p, (b) W 4f, (c) O1s, (d) Ag 3d, (e) I 3d, and (f) XPS survey pure $CuWO_4$, AgI and 2A/C

### *3.3.4. Optical bandgap studies*

A semiconductor's optical band gap is vital for understanding the photocatalytic mechanism. The band gap is found from the Tauc plot drawn using the solid-state UV-visible absorbance data. Expression (3.2) gives the Tauc relation.

$$(\alpha h\upsilon)^{1/n} = (h\upsilon - E_g) \qquad (3.2)$$

Here, α denotes the molar absorption coefficient, n is the transition exponent, and $E_g$ is the bandgap energy. An allowed direct transition has *n* equal to 0.5 for the allowed direct transition and 2 for the allowed indirect transition. The intercept of the linear fit to the plot on the x-axis gave the optical bandgap energy.

The Tauc plots of $CuWO_4$ and AgI exhibit two direct transition bandgaps at ~2.36 eV and 2.80 eV (Fig. 3.6). These values agree with the band gap values reported in the literature for pure $CuWO_4$ and AgI phases (Hassanien & Akl, 2015; Pal et al., 2020). We are investigating the bandgap of composite materials in which 20wt% of the second phase (AgI) is loaded on the major phase. $CuWO_4$ is the major phase and its average particle size was ~ 100 nm. The nanoparticles of the second (AgI) phase are finer and range between (30 nm). Thus, a small interface or contact area exists between the major and the second phase nanoparticles. The UV-visible reflectance is from the exposed surfaces of the nanoparticles of two phases. Hence, the composite solid-state UV-visible reflectance is just a superposition of the reflectance of pure phases in proportion to the exposed surfaces. However, deconvolution of such curves for finding the band gaps of respective phases is quite difficult and may not be accurate. Given the above discussion, band gaps have been calculated from the Tauc plots of pure phase nanoparticles for all composites. Note, for the sake of comparison, we have given the solid-state absorbance plots of all composites in all chapters.

Another critical piece of information needed for framing the photocatalytic mechanism is the VB and CB positions. These were calculated using the empirical formula proposed by Butler et al. (Walsh & Butler, 2014). Equations (3.3) and (3.4) give the expressions for these relations.

$$E_{vb} = \chi - E_0 + 0.5E_g \quad \text{----------(3.3)}$$

$$E_{cb} = E_{vb} - E_g \quad \text{----------(3.4)}$$

Here, $E_{vb}$ is the VB edge potential, the $E_0$ value is constant 4.5eV versus NHE, $E_{cb}$ is the CB position, $E_g$ is the semiconductor bandgap, and χ is the geometric mean of the electronegativities of atoms constituting the semiconductor. For the $CuWO_4$

component, the calculated VB position is +3.0eV, and its CB position is at 0.70eV. The VB position of AgI is at +2.36, and its CB is at -0.44eV.

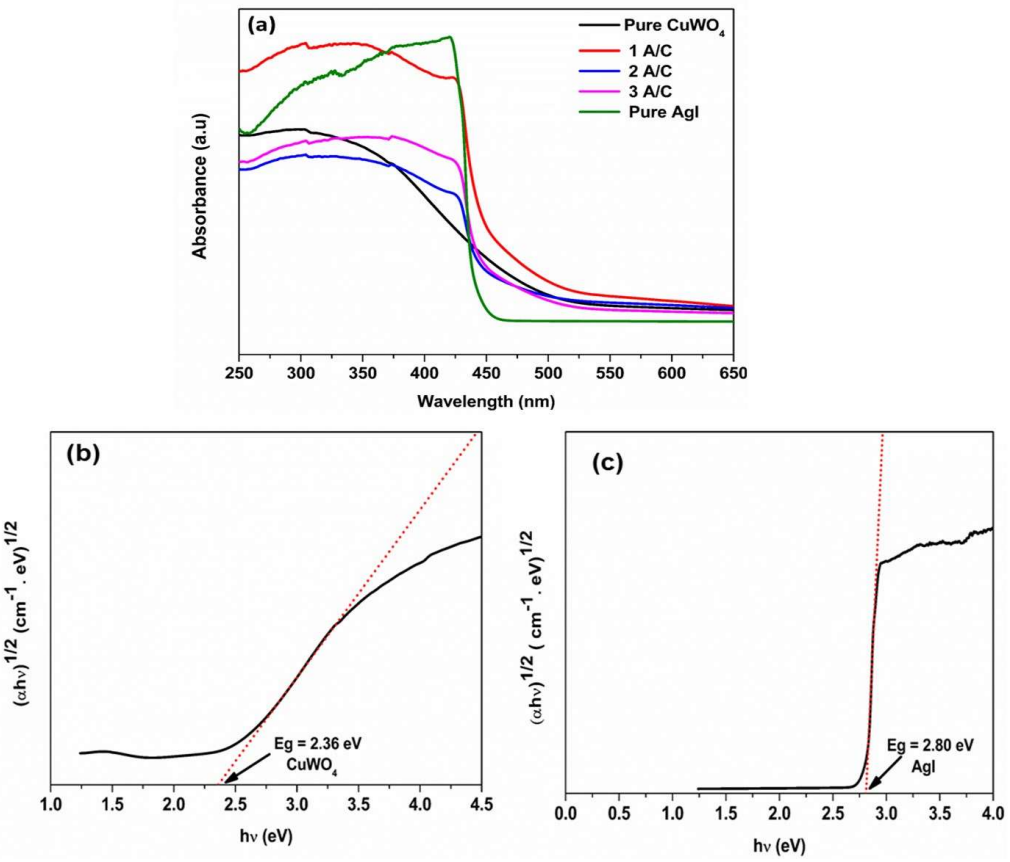


**Fig. 3.6: (**a) The solid-state UV−vis absorption spectrum of the nanomaterials prepared in this study. Plots of $(\alpha h\nu)^{1/2}$ vs. energy hν (Tauc plots) and bandgap energy of the pure b) $CuWO_4$ and c) AgI nanoparticles.

### *3.3.5. Photoluminescence properties*

Photoluminescence (PL) spectroscopy investigates the recombination of photo-induced charge carriers in photocatalysts. Lower PL intensities indicate lesser recombination. Fig. 3.7 shows the PL spectra of nanocomposites 1 A/C, 2 A/C, and 3 A/C. Pure $CuWO_4$ exhibits the highest PL intensity. The emission plot of 3A/C displays the next highest intensity and then the 1 A/C peak intensity. The peak intensity of the PL spectrum of sample 2 A/C is the minimum, indicating the least recombination and better photo-induced charge carrier separation in this nanocomposite (De et al., 2020). It appears

that less than optimum loading of AgI on the $CuWO_4$ nanostructures in 1 A/C causes this PL behavior. The recombination is least in 2 A/C because of the higher amount of AgI phase on $CuWO_4$. Finally, in 3 A/C, the nanocomposite AgI loading seems excessive and blocks light access to the $CuWO_4$ surface. In such a case, most of the time, only the AgI component gets photo-excited.

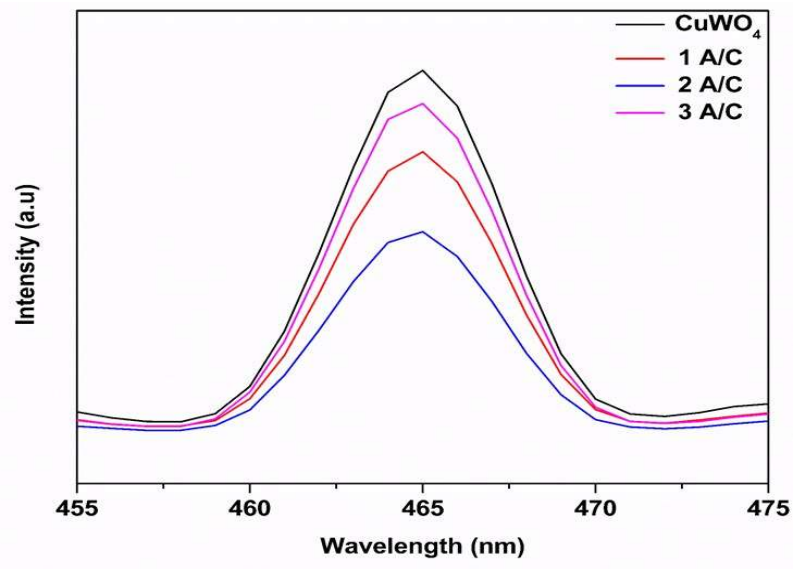


**Fig. 3.7:** Photoluminescence spectra of the prepared samples $CuWO_4$, 1 A/C, 2 A/C, and 3 A/C

### *3.3.6. Evaluation of photocatalytic activity*

The nanocomposites showed photocatalytic activity for RhB and CIP degradation under visible light. The details of the photocatalytic degradation of RhB and CIP are shown in Fig. 3.8. The nanocomposites displayed better photocatalytic degradation activities (for both CIP and RhB) than pure AgI or $CuWO_4$ nanoparticles (Fig. 3.9). Nanocomposite 2 A/C showed the best photocatalytic activity. Relatively, the degradation of RhB and CIP was slower on 1 A/C. However the degradation activity was least for 3 A/C among the nanocomposites. The observed trend is as per PL spectrum intensity order. Thus, photocatalysts with lesser recombination show better photocatalytic activities for RhB and CIP degradation.

The absorption maximum of the RhB spectrum demonstrates a blue shift during its visible light photocatalytic degradation. This observation is widely reported in the literature. Rhodamine B is a dye with a maximum absorption peak ($\lambda_{max}$) at 554 nm. Hence, RhB also gets photo-excited when exposed to cool white LED visible light irradiation. However, the $\lambda_{max}$ of an aqueous solution of Rhodamine B does not change as a function of time when exposed to visible light. The change in $\lambda_{max}$ of Rhodamine B occurs only during photocatalysis, implying a photosensitizer role for RhB. Reference [Journal of Photochemistry & Photobiology, A: Chemistry 433 (2022) 114176] has investigated this issue. These authors concluded that the N-de-ethylation process was primarily due to photo-excited electron transfer from the RhB molecule to the photocatalyst. N-de-ethylation from RhB, i.e., the four ethyl groups of the RhB molecule, occurs in a stepwise manner (Yang & Yang, 2018).

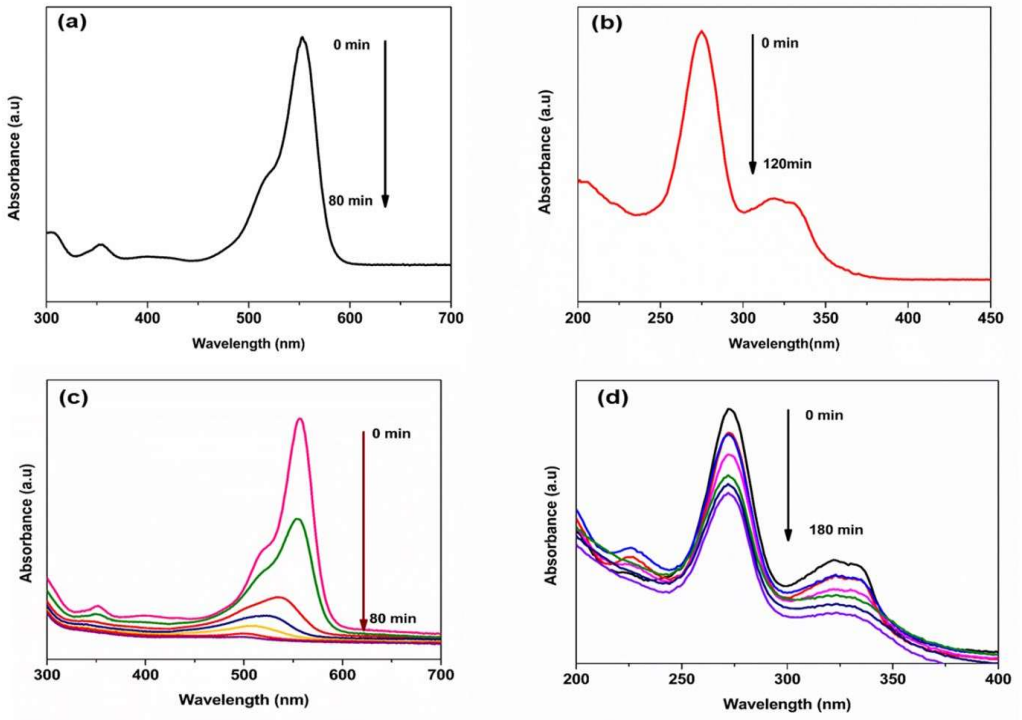


**Fig. 3.8:** (a) and (b) show photolysis of Rhodamine and ciprofloxacin without catalysts. (c) and (d) shows, UV Visible spectral change of Rhodamine and CIP under light exposure using 2 A/C catalyst

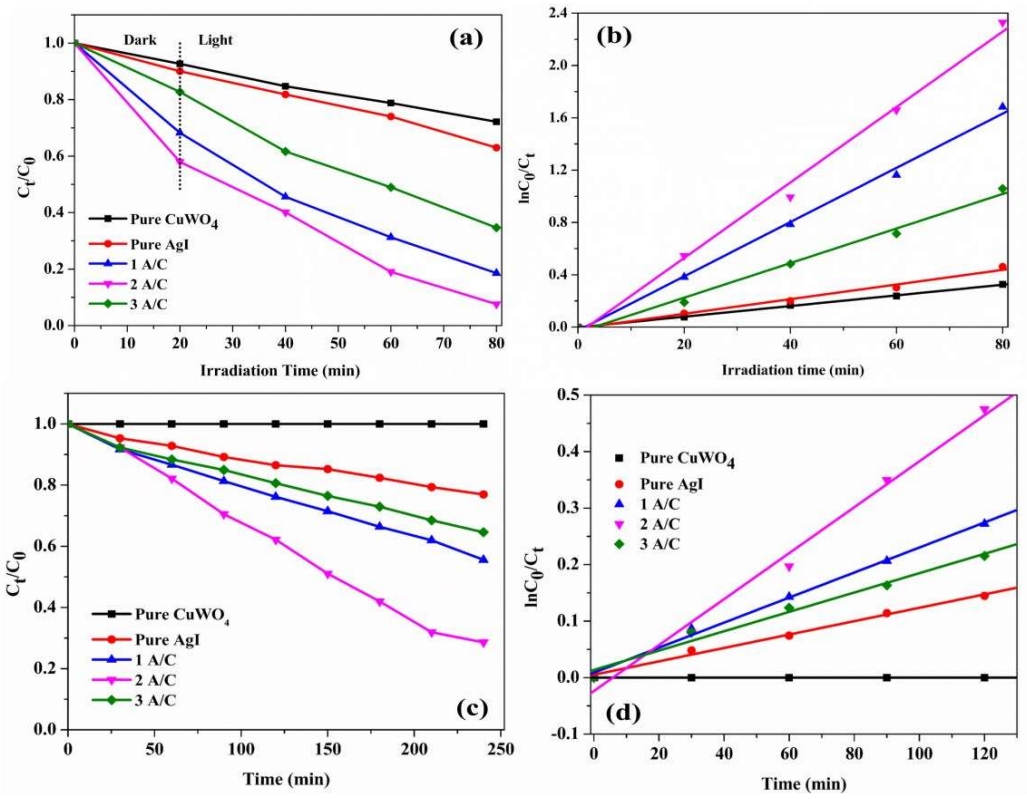


**Fig. 3.9:** (a) Comparison chart for degradation efficiency by different catalysts for RhB degradation, (b) Rate constants (k) and first-order kinetics of $CuWO_4$ and AgI 1 A/C, 2 A/C, 3 A/C nanocomposites for Rhodamine degradation, (c) A comparison of CIP degradation with time over the investigated photocatalysts, (d) CIP degradation over the prepared nanoparticles fit first-order kinetics

The photocatalytic degradation of both CIP and RhB followed first-order kinetics (Fig. 3.9). Note that accurate determination of the kinetics of a reaction requires data from the initial stages of the reaction. In other words, when the product formed is not appreciable compared to the reactant concentration (Leidler, 1987). This is why fewer data points exist in the kinetic plot Fig. 3.9(d). The details of RhB and CIP degradation kinetics are given in Tables 3.1 and 3.2. Table 3.3 and 3.4 compares the CIP and RhB degradation turnover frequency (TOF) for the 2 A/C photocatalyst with those published earlier in the literature, respectively.

**Table 3.1**: Rate constant ($k$) and correlation coefficient ($R^2$) for CIP degradation on pure $CuWO_4$, AgI, 1A/C, 2A/C, and 3A/C photocatalysts.

| Catalysts | Apparent rate constant ($min^{-1}$) | $R^2$ |
|---|---|---|
| Pure $CuWO_4$ | $7.88\times10^{-5}$ | 0.841 |
| Pure AgI | $5.3\times10^{-5}$ | 0.954 |
| 1 A/C | $6.6\times10^{-4}$ | 0.994 |
| 2 A/C | $1.06\times10^{-2}$ | 0.998 |
| 3 A/C | $2.41\times10^{-4}$ | 0.989 |

**Table 3.2:** Rate constant ($k$) and correlation coefficient ($R^2$) for RhB degradation on pure $CuWO_4$, AgI, 1A/C, 2A/C, and 3A/C photocatalysts.

| Catalysts | Apparent rate constant ($min^{-1}$) | $R^2$ |
|---|---|---|
| Pure $CuWO_4$ | $4.0\times10^{-3}$ | 0.999 |
| Pure AgI | $5.8\times10^{-4}$ | 0.984 |
| 1A/C | $1.8\times10^{-2}$ | 0.994 |
| 2A/C | $2.8\times10^{-2}$ | 0.997 |
| 3A/C | $1.2\times10^{-2}$ | 0.988 |

**Table 3.3:** CIP degradation turnover frequency (TOF) values over different photocatalysts with 2 A/C.

| Photocatalysts | Light source | Turn over frequency ($mol.g^{-1}.min^{-1}$) | References |
|---|---|---|---|
| $Bi_2S_3$/BiOBr | 300W Xe lamp | $2.6\times10^{-4}$ | (Y. Hong et al., 2017) |
| AgI/BiOBr | 300W Xe lamp | $9\times10^{-4}$ | (Yu et al., 2018) |
| $WO_3$/BiOBr | 300W Xe lamp | $4.7\times10^{-4}$ | (Ling & Dai, 2020) |
| AgI/$CuWO_4$ | Cool white LED (1070 $W/m^2$) | $5\times10^{-4}$ | This work |

**Table 3.4.** Comparison of RhB degradation turnover frequency (TOF) values over different photocatalysts with 2 A/C.

| Photocatalysts | Light source | Turnover frequency ($mol.g^{-1}.min^{-1}$) | References |
|---|---|---|---|
| AgI/ZnO | 300W Xe lamp | $1.2\times10^{-3}$ | (Shaker-Agjekandy & Habibi-Yangjeh, 2015) |
| AgI/g-$C_3N_4$ | 500W Xe lamp | $2.5\times10^{-3}$ | (Huang et al., 2021) |
| $Ag_3PO_4/Ag_2MoO_4$ | 300W Xe lamp | $7.7\times10^{-3}$ | (Cao et al., 2017) |
| AgI /$CuWO_4$ | Cool white LED (1070 $W/m^2$) | $4.3\times10^{-3}$ | This work |

### *3.3.7. Reusability of photocatalysts*

Fig. 3.10a shows the stability and reusability of photocatalysts AgI/$CuWO_4$ under visible light irradiation. Recyclability experiments were conducted only on 2 A/C photocatalysts, considering their enhanced photocatalytic activity. Experimental conditions were identical in all cycles. The 2 A/C photocatalyst recyclability was ~80% (relative to the product formed in the first cycle) even after the 5$^{th}$ cycle. This decrease in photocatalytic efficiency after the 5$^{th}$ cycle of reuse could be due to some photocatalyst degradation (Guo et al., 2019). Accordingly, an XRD was conducted on the 2 A/C after its repeated use for RhB degradation. Fig. 3.12 shows this XRD after the recyclability test. The AgI and $CuWO_4$ phase peaks in the XRD remained intact after repeated photocatalyst use. Ag-based phases have been known to undergo photo corrosion under repeated use; therefore, the leaching of Ag from AgI could also cause a decrease in CIP degradation efficiency. An ICP analysis was done to investigate this issue. The concentration of Ag element in the tested 2 A/C sample decreased by nearly 20% from (1$^{st}$ cycle) 151 ppm to 121 ppm by the end of the 5$^{th}$ cycle (Fig. 3.12). Thus,

the decrease in photocatalytic efficiency is because of Ag leaching from the photocatalyst during reuse.

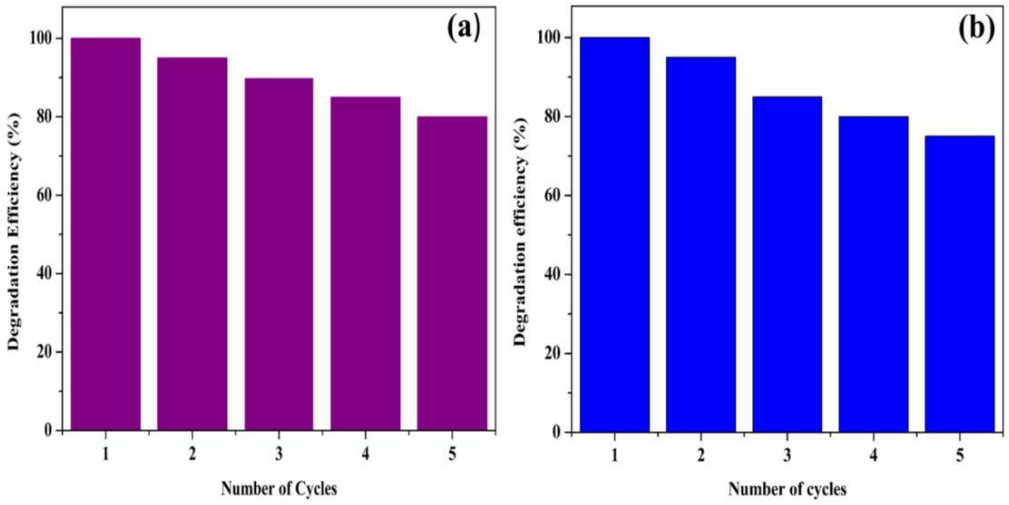


**Fig. 3.10:** (a) Recycling efficiency of 2 A/C photocatalyst during the degradation of CIP process, (b) recycling efficiency of 2 A/C photocatalyst during the RhB degradation process.

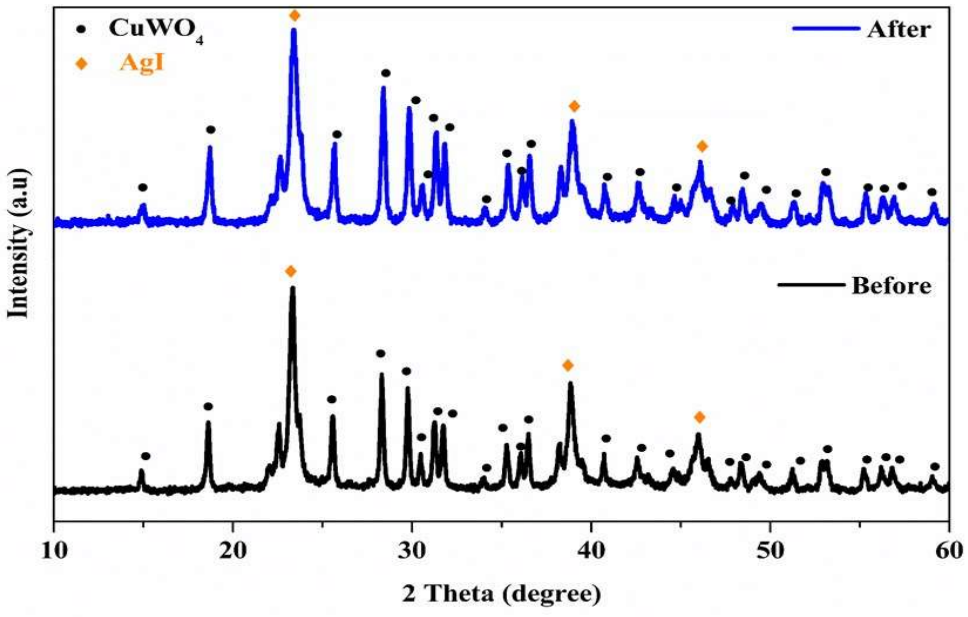


**Fig. 3.11:** XRD of sample 2/A/C after five cycles of reuse

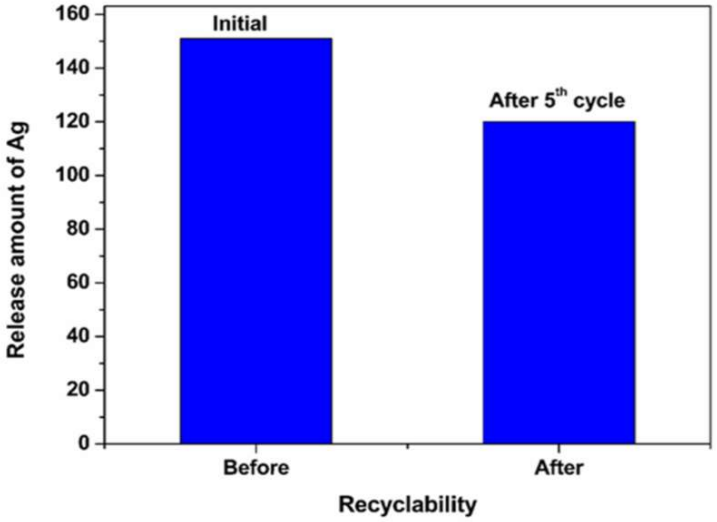


**Fig. 3.12:** The amount of Ag element in the 2 A/C photocatalyst sample before and after five cycles of its reuse for CIP degradation experiments

### *3.3.8. Scavenger test*

Several control experiments with different free radical scavengers were performed on 2 A/C nanocomposite under visible light irradiation. These experiments helped detect the reactive species and elucidate the photocatalytic mechanism. Separate experiments were conducted with KI as the hole scavenger, IPA as the $^{\bullet}OH$ radical scavenger, and PBQ for scavenging $O_2^{\bullet-}$ (superoxide species) in the reaction mixture (Kumar et al., 2019). Fig. 3.13 compares the reaction in the presence and absence of the scavenger. All reactions were carried out under the same experimental conditions. The only change was the scavenger. The rest of the inputs remained the same in all experiments. Fig. 3.13a gives the percentage of the substrate (CIP) degraded in three hours in the presence of various scavengers relative to that obtained without any scavenger. The first bar in this figure denotes the experiment carried out without any scavenger (labeled as Blank). The first bar is the benchmark and is assumed to be 100%. The second, third, and fourth bars represent the relative (to the first bar) percent of degradation observed when the reaction was carried out in the presence of IPA, KI, and PBQ, respectively. Both for RhB (Fig. 3.13b) and CIP degradation, the reaction kinetics were inhibited most by

PBQ. Thus, the superoxide radical was the predominant active species during the reaction on the 2 A/C nanocomposite. For CIP degradation KI also inhibited the reaction, but the extent was lesser than for the superoxide species. The hydroxyl radical participation was minimal during CIP degradation. In contrast, the effect of IPA (the scavenger for hydroxyl radicals) on RhB degradation (Fig. 3.13b) was more than that observed when the same reaction was carried out in the presence of KI.

In another control experiment, water was replaced by acetonitrile. The purpose was to find the effect of water on CIP degradation. The reaction was conducted under continuous oxygen purging (with acetonitrile as the solvent). Other experimental variables remained the same. No CIP degradation was observed under these conditions.

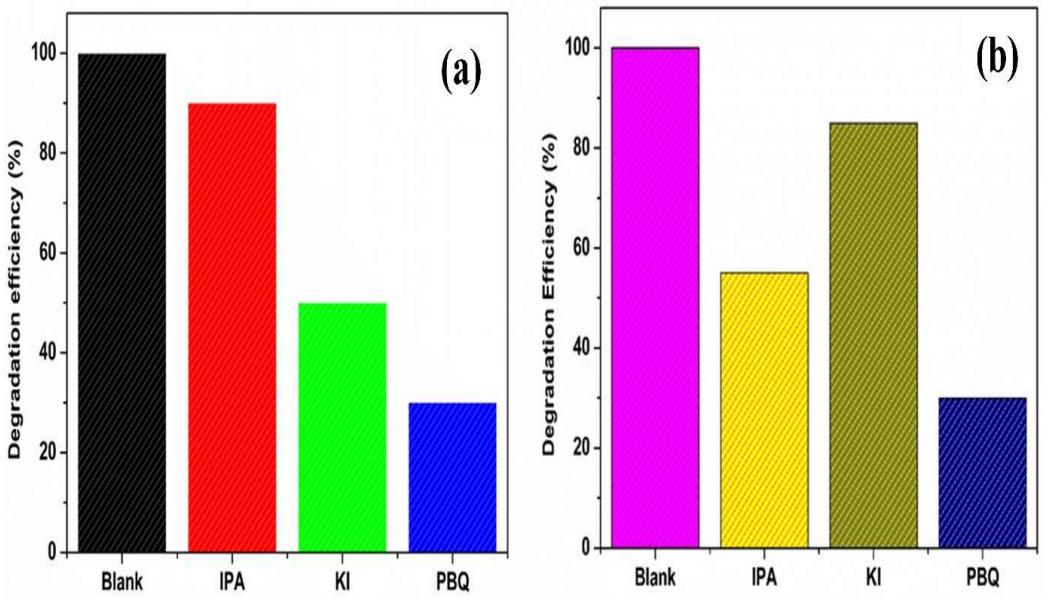


**Fig. 3.13:** Photocatalytic degradation of (a) CIP and (b) RhB over 2 A/C in the presence of different active species scavengers

### *3.3.9. Photocatalytic reaction mechanism*

Irradiation of the 2 A/C photocatalyst with visible light excites electrons from the VBs of both $CuWO_4$ and AgI components. Simultaneously, the photoexcited electrons in the CB of the $CuWO_4$ migrate to the VB of the AgI component. Overall, photo-excited holes remain in the VB of $CuWO_4$, and electrons are transferred to the CB of AgI. The XPS results demonstrated the charge migration from the $CuWO_4$ side to the AgI part (see discussion in section 3.2). AgI's highly negative CB facilitates superoxide active species formation.

The degradation of CIP and RhB in the presence of PBQ inhibits the reaction, indicating that $O_2^{\bullet-}$ is the main active species during the reaction. The scavenger results for CIP degradation show that PBQ affects the photocatalyst the most. But KI (the hole scavenger) also influences the kinetics quite severely. Previous literature also suggests that water oxidation occurs on the $CuWO_4$ part. The above information indicates that CIP and water oxidation feed electrons to the photoexcited holes on $CuWO_4$.

For RhB, the scavenger for hydroxyl radicals affects the degradation kinetics the most after superoxide radicals. A non-selective product of the one-electron superoxide radical reduction ($O_2^{\bullet-} + e^- + 2H^+ \rightarrow H_2O_2$) can produce $H_2O_2$. The reductive cleavage of such $H_2O_2$ molecules would produce hydroxyl radicals. The possibility of hydroxyl radical generation by hole oxidation of hydroxide anion ($OH^- + h^+ \rightarrow {}^{\bullet}OH$) does not arise because the reaction occurs under acidic pH conditions (Yang et al., 2017). Hence, the IPA scavenger consumes the hydroxyl radicals generated from superoxide radicals and inhibits RhB degradation. Fig. 3.14 summarizes the possible photocatalytic mechanisms over the cost-effective Z-scheme 2 A/C photocatalyst.

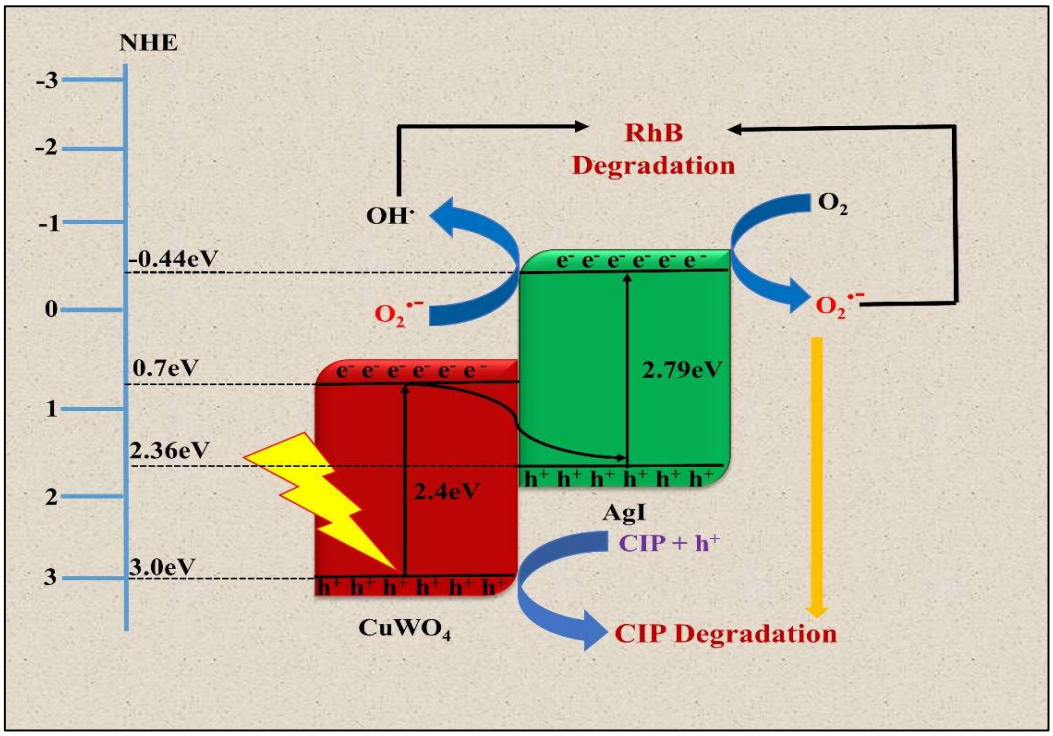


**Fig. 3.14:** Proposed Z-Scheme mechanism of the photocatalytic process involved in CIP and RhB degradation by 20% A/C

### 3.4. Conclusions

$AgI/CuWO_4$ nanocomposites prepared by a stage-wise precipitation route are found to be efficient visible-light photocatalysts for CIP and RhB degradation. HR-TEM and elemental mapping confirmed the precipitation of AgI structures on $CuWO_4$ nanoparticles. The nanocomposite with 20% (by weight) AgI loading on $CuWO_4$ nanostructures gave optimum PL and photocatalytic activity results. XPS analysis of the 2 A/C nanocomposite demonstrated charge transfer from the $CuWO_4$ side to the AgI part, signifying a Z-scheme mechanism. The active species trapping analysis revealed that the superoxide species were primarily responsible for CIP and RhB degradation.